

The effect of tides on the Fornax dwarf spheroidal galaxy

Giuseppina Battaglia^{1,2*}, Antonio Sollima³ and Carlo Nipoti⁴

¹*Instituto de Astrofísica de Canarias, calle Via Lactea s/n, 38205 La Laguna, Tenerife, Spain*

²*Universidad de La Laguna, Dpto. Astrofísica, 38206 La Laguna, Tenerife, Spain*

³*INAF - Osservatorio Astronomico di Bologna, via Ranzani 1, 40127 Bologna, Italy*

⁴*Department of Physics and Astronomy, University of Bologna, Viale Berti Pichat 6/2, 40127 Bologna, Italy*

Accepted 2015 September 07. Received 2015 September 03; in original form 2015 August 06.

ABSTRACT

Estimates of the mass distribution and dark-matter (DM) content of dwarf spheroidal galaxies (dSphs) are usually derived under the assumption that the effect of the tidal field of the host galaxy is negligible over the radial extent probed by kinematic data-sets. We assess the implications of this assumption in the specific case of the Fornax dSph by means of N -body simulations of a satellite orbiting around the Milky Way. We consider observationally-motivated orbits and we tailor the initial distributions of the satellite’s stars and DM to match, at the end of the simulations, the observed structure and kinematics of Fornax. In all our simulations the present-day observable properties of Fornax are not significantly influenced by tidal effects. The DM component is altered by the interaction with the Galactic field (up to 20% of the DM mass within 1.6 kpc is lost), but the structure and kinematics of the stellar component are only mildly affected even in the more eccentric orbit (more than 99% of the stellar particles remain bound to the dwarf). In the simulations that successfully reproduce Fornax’s observables, the dark-to-luminous mass ratio within 1.6 kpc is in the range 5 – 6, and up to 16 – 18 if measured within 3 kpc.

Key words: dark matter – galaxies: dwarf – galaxies: individual: Fornax – galaxies: kinematics and dynamics – galaxies: structure

1 INTRODUCTION

Over the years, the manifold growth in the size of spectroscopic samples of individual stars has allowed the determination of accurate and spatially extended line-of-sight (LOS) velocity-dispersion profiles for each of the Milky Way (MW) “classical” dwarf spheroidal galaxies (dSphs¹; e.g. Kleyna et al. 2001; Koch et al. 2007; Walker et al. 2007; Battaglia et al. 2008; Muñoz et al. 2006; Battaglia et al. 2011; Walker 2013) as well as of higher moments of the LOS velocity distribution (e.g. Lokas 2009; Breddels et al. 2013; Breddels & Helmi 2013, hereafter BH13; Richardson & Fairbairn 2014). Equilibrium dynamical modeling of these data-sets leads to the finding that MW dSphs exhibit some of the most extreme dynamical mass-to-light (M/L) ratios known to-date, up to several 100s (M/L)_⊙. This has triggered a large body of works attempting to assess the dark matter (DM) content and distribution of these galaxies (for recent reviews see Battaglia, Helmi & Breddels 2013; Strigari 2013; Walker 2013), which is an important piece of information to un-

derstand the nature of DM particles (e.g. Ackermann et al. 2014) and to test the predictions of cosmological models of galaxy formation, for instance regarding the mass function of luminous satellites around MW-like systems (e.g. Klypin et al. 1999; Moore et al. 1999) and the effects of baryons on the DM distribution (e.g. Navarro et al. 1996; Nipoti & Binney 2015, Zolotov et al. 2012).

However, it has always been a matter of debate whether the tidal interaction experienced by these small galaxies during their orbital evolution around the MW may have impacted their dynamical status to the extent of significantly altering estimates of their current DM content and distribution. Observational evidence of on-going tidal disturbance in some M31 satellite galaxies is provided by the clear presence of tidal tails or strong structural distortions (e.g. Choi, Guhathakurta, & Johnston 2002; McConnachie et al. 2010; Crnojevic et al. 2014). Around the MW, beside the spectacular case of Sagittarius (e.g. Ibata, Gilmore, & Irwin 1994), several “ultra-faint” dwarf galaxies exhibit distorted or very elongated morphologies (e.g. the Hercules dSph; Roderick et al. 2015) however, among the “classical” dSphs, only Carina shows clear signs of tidal disturbance in its structural properties (Muñoz et al. 2006; Battaglia et al. 2012; McMonigal et al. 2014). Given the difficulties in detecting low-surface

* E-mail: gbattaglia@iac.es

¹ We refer to the dSphs known prior to the SDSS as “classical” dSphs, while those discovered afterwards as “ultra-faint dwarfs”.

brightness tidal features from stellar counts in objects as faint and extended on the sky as the MW dSphs, it is still not excluded that such non-detections may be due to the lack of appropriately deep and spatially extended photometric data-sets.

A tumultuous past, marked by strong mass loss due to interactions with the host, is expected also from a theoretical point of view, in order to explain the present-day properties of the observed population of MW satellite galaxies in a well-motivated cosmological framework (e.g. Sawala et al. 2014; Barber et al. 2015), and even more so in those models that explain dSphs as the result of “tidally stirred” dwarf disc galaxies (e.g. Mayer et al. 2001, Kazantzidis et al. 2011, Tomozeiu, Mayer, & Quinn 2015).

In general, as long as the satellite galaxy retains a bound core, the LOS velocity dispersion of the stars in the central regions remains a good indicator of the maximum circular velocity and bound mass (e.g. Muñoz, Majewski, & Johnston 2008; Peñarrubia, Navarro, & McConnachie 2008; Klimentowski et al. 2009; Kazantzidis et al. 2011). At larger projected radii, however, stars originating in the tidal tails may contaminate kinematic samples of individual stars in MW dSphs, inflating their measured velocity dispersions and significantly altering the DM content and distribution inferred from an equilibrium dynamical analysis (e.g. Klimentowski et al. 2007, Read et al. 2006; Muñoz, Majewski, & Johnston 2008).

The amount of tidal disturbance experienced is obviously dependent on the orbital history of the satellite. However, even if an object has suffered a large degree of mass loss, this does not necessarily imply lack of current dynamical equilibrium. Tidally perturbed stars progressively become unbound and are eventually dispersed, with the object eventually settling in a new equilibrium configuration (Peñarrubia et al. 2009). Also, the degree of contamination of kinematic data-sets from stars originating in tidal tails can vary along the orbit, as a consequence of the varying orientation of the inner regions of the tidal tails with respect to the LOS (e.g. Klimentowski et al. 2009). Given the difficulty in unambiguously identifying unbound stars lingering close to the main body of the MW dSphs, it is quite possible that, depending on the specific orbital history and current location along the orbit, the observed kinematics of stars is a faithful tracer of their underlying potential in some of the MW dSphs and not in others.

N -body simulations tailored to reproduce the present-day position and systemic velocity, as well as the observed structural and internal kinematic properties of *specific* MW dSphs appear particularly well suited to explore this issue. Such an approach has been for example applied to Carina (Muñoz et al. 2006) and Leo I (Sohn et al. 2007, Mateo, Olszewski, & Walker 2008), for which it was shown that modeling these galaxies as tidally disturbed systems initially embedded in “mass-follows-light” DM halos, rather than in extended halos, yields a good match to the data. The inferred DM content is much lower than what inferred from a Jeans analysis in the hypothesis of dynamical equilibrium (from $24(M/L)_{\odot,V}$ in Koch et al. 2007 to $\sim 5(M/L)_{\odot,V}$ in Sohn et al. 2007, for Leo I; from $80(M/L)_{\odot,V}$ in Walker et al. 2007 down to $\sim 40(M/L)_{\odot,V}$ in Muñoz, Majewski, & Johnston 2008 for Carina). The orbits that provide the best match to the data have small perigalacticons and high eccen-

tricity. While for Carina this is in good agreement with the inferences from the measured proper motion (Piatek et al. 2003), it is likely that Leo I orbit has a larger perigalacticon distance, 91 ± 36 kpc (Sohn et al. 2013). Hence the impact of tidal interaction with the MW might have been significantly over-estimated for this galaxy.

For investigations of the dynamical status of the MW dSphs, it is therefore advisable to focus on modeling objects placed on observationally motivated orbits. In this work, we take under consideration the Fornax dSph. There is consensus that this object is moving on a rather external orbit around the MW (Dinescu et al. 2004; Piatek et al. 2007, hereafter P07; Méndez et al. 2011), so Fornax is a good candidate of dSph that might be close to equilibrium. Our aim is to quantify the effects of tides on Fornax’s structure and kinematics, by means of N -body simulations following the evolution in the MW of a satellite dwarf galaxy, similar in structure to Fornax, on orbits that are consistent with the current observational constraints, including Fornax’s proper motions. The Fornax dSph is also one of the best studied MW dSphs, hence we can then rely on a comprehensive set of observational properties against which to compare the models.

We review the relevant set of observables in Section 2. In Section 3 we describe the set-up of the N -body simulations, whose results are shown in Section 4. We conclude with a summary in Section 5.

2 THE FORNAX DWARF SPHEROIDAL GALAXY: OBSERVED PROPERTIES

The N -body simulations used in this work have been set up in order to reproduce the main observables of the Fornax dSph. Concerning the structural properties of the stellar component, we focus on reproducing the measured stellar mass and observed surface number density profile, while for the internal kinematics we focus on the observed LOS velocity-dispersion profile. The simulated object is also required to have present-day projected position, heliocentric distance, systemic radial velocity and systemic proper motion similar to the observed ones.

The Fornax dSph appears to have a regular, well-behaved 2D stellar distribution, with constant ellipticity $\epsilon \simeq 0.3$, as revealed by spatially extended photometric data reaching down to the base of the red giant branch (RGB; e.g. Battaglia et al. 2006; see Bate et al. 2015 for a recent, panoramic view over a 25 deg^2 region around Fornax based on VST/ATLAS data). The only sign of irregularity at large spatial scales was claimed by Coleman et al. (2005), who detected a shell-like feature outside Fornax’s nominal King tidal radius ($\simeq 3.25$ kpc) in the distribution of RGB stars along the minor axis. The deeper imaging survey by Bate et al. (2015) showed that this feature is a mis-identified overdensity of background galaxies. In the inner regions the stellar distribution shows departures from elliptical symmetry (Irwin & Hatzidimitriou 1995), which are very likely due to the asymmetric spatial distribution of the young main sequence stars (see Stetson, Hesser, & Smecker-Hane 1998; Battaglia et al. 2006; de Boer et al. 2013). There are also a number of small stellar substructures in the spatial distribution and kinematics of the stars within 0.3 deg (Coleman et

al. 2004; Battaglia et al. 2006; Olszewski et al. 2006; de Boer et al. 2013), some of which may be related to the accretion of a smaller stellar system and others simply to patchy recent star formation. All of the above signs of irregularity do not require the occurrence of significant tidal effects.

Fornax’s distance modulus has been derived from various techniques - optical photometry of the horizontal branch, the tip of the RGB, RR Lyrae stars, red clump (RC) stars, as well as from near-infrared photometry of the RC and RGB tip (Pietrzyński et al. 2009 and references therein). These are all in good agreement within the typical standard and systematic errors, yielding an average value of ~ 140 kpc, very close to the value here adopted, i.e. $d = 138 \pm 8$ kpc (Saviane, Held, & Bertelli 2000).

We take as reference the ellipticity ϵ , position angle (P.A.) and observed surface number-density profile from Battaglia et al. (2006), who used relatively deep ESO/WFI V & I photometry extending out to Fornax’s nominal King tidal radius to study the structure of this galaxy. The observed surface number density as a function of circularized² radius is best fit by a Sérsic (1968) profile

$$I(R) = I_0 \exp \left[- \left(\frac{R}{R_S} \right)^{1/m} \right] \quad (1)$$

with $R_S = 14.5'$ ($\simeq 0.58$ kpc, at a distance of 138 kpc) and $m = 0.71$. For these values of R_S and m the projected circularized radius containing half of the total number of stars is $\simeq 0.62$ kpc.

The stellar mass of Fornax was estimated by de Boer et al. (2012) who performed a star formation history determination over a wide area using what are so far the deepest available color-magnitude diagrams over a large spatial region for this galaxy. The resulting stellar mass is $4.3 \times 10^7 M_\odot$ within a projected circularized radius 0.66 deg (1.6 kpc). The observed LOS velocity dispersion profile was derived by M. Breddels from ~ 2900 individual probable Fornax members following the approach outlined in BH13, but binning stars in elliptical annuli³.

A central information to our analysis is the one provided by the systemic heliocentric velocity and proper motion of Fornax, which determines the orbit of the object around the MW and allows us to understand how important tidal effects may have been in the evolution of this galaxy. In the literature there is good consistency among the heliocentric LOS systemic velocity ($v_{\text{sys,h}}$) values derived from different spectroscopic data-sets of individual stars, even though the samples have widely different sizes and were gathered at various observing facilities (e.g. $v_{\text{sys,h}} = 53 \pm 1.8, 54.1 \pm 0.5, 53.3 \pm 0.8 \text{ km s}^{-1}$ from Mateo et al. 1991, Battaglia et al. 2006, Walker et al. 2006, respectively).

There are several direct estimates of the systemic proper

² In the literature the observed properties of Fornax are often reported as functions of the semi-major axis a (also called “elliptical radius”). In this work, in both observations and simulations, we always refer to the circularized radius $R \equiv \sqrt{ab} = a\sqrt{1-\epsilon}$, where b is the semi-minor axis and ϵ is the ellipticity. In particular, given the observed ellipticity $\epsilon = 0.3$, the circularized Sérsic radius $R_S = 14.5'$ corresponds to an elliptical radius $17.3'$.

³ The LOS velocity dispersion profile published in BH13 differs from the one used here, because BH13 binned the data in circular annuli.

Table 1. Values of Fornax’s observational parameters adopted in this work. The position angle, P.A., is defined as the angle between the North and the projected major axis of the galaxy measured anti-clockwise. The systemic velocity $v_{\text{sys,h}}$ refers to the heliocentric reference frame, while the radial (v_r) and tangential (v_t) velocity components are in the Galactocentric system. The quoted radii are circularized projected radii. References: 1) Mateo (1998); 2) Battaglia et al. (2006); 3) de Boer et al. (2012); 4) Saviane, Held, & Bertelli (2000); 5) Piatek et al. (2007).

(l,b)	(237.1°, −65.7°)	1
ϵ	0.3±0.01	2
P.A.	46.8° ± 1.6°	2
R_S	14.5 arcmin	2
m	0.71	2
$M_*(R < 1.6 \text{ kpc})$	$4.3 \times 10^7 M_\odot$	3
d	138±8 kpc	4
$v_{\text{sys,h}}$	$54.1 \pm 0.5 \text{ km s}^{-1}$	2
v_r	$-31.8 \pm 1.7 \text{ km s}^{-1}$	5
v_t	$196 \pm 29 \text{ km s}^{-1}$	5

motion of Fornax from astrometric measurements (Dinescu et al. 2004; Piatek et al. 2007, hereafter P07; Méndez et al. 2011), which are somewhat discrepant (see table 6 of Méndez et al. 2011). For example, the current range of most likely apogalacticon estimates is very wide, from 152 kpc (P07) reaching up to the 965 ± 356 kpc as from the work of Méndez et al., in which case Fornax would be at its first pericentric passage. However, all measurements consistently suggests that Fornax is unlikely to have passed close to the MW centre, as the most likely perigalacticons range from 118 kpc (P07) to 148 kpc (Méndez et al. 2011). As we wish to assess the impact of tidal disturbances, we adopt the orbital parameters from P07, which yield the tightest orbit among the direct proper motion measurements. This determination is also in very good agreement with indirect proper motion determinations from stellar redshifts (Walker et al. 2008).

The values of Fornax’s observational parameters adopted in this paper are summarized in Table 1.

3 SET-UP OF THE N -BODY SIMULATIONS

In order to study the effect of tides on the internal structure and kinematics of Fornax we ran a set N -body simulations of a Fornax-like object in orbit around the MW. In the simulations the MW is represented as a fixed gravitational potential: in particular we adopt the Galactic potential of Johnston, Spergel, & Hernquist (1995), which consists of a Miyamoto & Nagai (1975) disc

$$\phi_{\text{disc}} = - \frac{G M_{\text{disc}}}{\sqrt{R^2 + (a + \sqrt{z^2 + b^2})^2}}, \quad (2)$$

a spherical Hernquist (1990) bulge

$$\phi_{\text{bulge}} = - \frac{G M_{\text{bulge}}}{r + c}, \quad (3)$$

and a logarithmic DM halo

$$\phi_{\text{halo}} = v_{\text{halo}}^2 \ln(r^2 + d_{\text{halo}}^2), \quad (4)$$

where r is the Galactocentric radial spherical coordinate, and R and z are the Galactocentric radial and vertical cylindrical coordinates. We adopt $M_{\text{disc}} = 10^{11} M_\odot$, $M_{\text{bulge}} =$

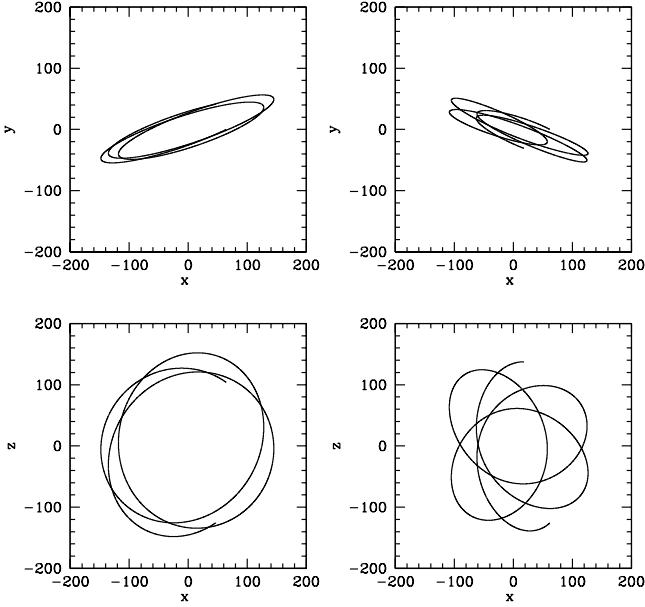


Figure 1. Paths of the P07best (left-hand panels) and P07ecc (right-hand panels) orbits integrated in the MW potential for 12 Gyr up to the present-day position of Fornax. Here x , y and z are Cartesian Galactocentric coordinates in units of kpc (z is orthogonal to the Galactic plane).

$3.4 \times 10^{10} M_{\odot}$, $v_{\text{halo}} = 128 \text{ km s}^{-1}$, $a = 6.5 \text{ kpc}$, $b = 0.26 \text{ kpc}$, $c = 0.7 \text{ kpc}$ and $d_{\text{halo}} = 12 \text{ kpc}$. This Galactic model has been previously used in many other studies focused on the determination of orbits of globular clusters (Dinescu et al. 2000; Allen, Moreno, & Pichardo 2008) and by P07 to calculate the orbit of Fornax.

The phase-space coordinates of the centre of mass of the simulated satellite at the beginning of the simulations have been derived by taking a test particle with the present-day phase-space coordinates of Fornax’s centre and evolving it backward in time for 12 Gyr in the adopted Galactic potential. In order to take into account the uncertainties in the estimated proper motions, we considered two different orbits: *i*) the best-fitting orbit inferred by P07 (hereafter, “orbit P07best”); *ii*) the most eccentric (i.e. with the smallest perigalacticon) orbit compatible within 3σ with the observed radial velocity and proper motions by P07 (hereafter, “orbit P07ecc”). The paths of the two considered orbits are shown in Fig. 1: the orbit P07best is an almost polar orbit, with perigalacticon $r_p = 118 \text{ kpc}$ and apogalacticon $r_a = 152 \text{ kpc}$, yielding an orbital eccentricity $e = (r_a - r_p)/(r_a + r_p) \simeq 0.13$; the P07ecc orbit has eccentricity $e \simeq 0.4$ and perigalactic radius $r_p = 61 \text{ kpc}$. Over the considered 12 Gyr the dwarf galaxy goes through three pericentric passages in orbit P07best and five pericentric passages in orbit P07ecc.

In the initial conditions of the simulations Fornax is represented with particles as a two-component, spherically symmetric system: a stellar component embedded in a DM halo. This is an approximation, since Fornax’s stellar component is observed to be mildly flattened, with projected ellipticity ~ 0.3 (in Section 4.4 we will present a simulation in which we attempt to reproduce also the observed

ellipticity). The initial structure of the satellite has been chosen so that at the end of the simulation (after 12 Gyr) the satellite has projected stellar-density and LOS velocity-dispersion profiles similar to those observed for Fornax (see Section 2). Of course, the problem of matching the final snapshot of the simulations with the observations is degenerate and requires some assumptions to limit the number of free parameters. In particular we assumed that the initial velocity distributions of stars and DM in the satellite are isotropic, and we also fixed the functional form of the initial stellar and DM density profiles.

The initial stellar component of the dwarf is a spherical distribution with density profile (Lima Neto, Gerbal, & Márquez 1999)

$$\rho_* = \rho_{0,*} \left(\frac{r}{r_{c,*}} \right)^{-p} e^{-\left(\frac{r}{r_{c,*}} \right)^{\nu}}, \quad (5)$$

which for $\nu = 1/m$ and $p = 1 - 0.6097\nu + 0.05463\nu^2$ is a good approximation of the deprojection of the Sérsic (1968) profile (equation 1) with index m and characteristic radius $r_{c,*} = R_S$. The density profile of the DM halo is not strongly constrained by the available observations: in particular it is uncertain whether the central DM density profile is cuspy or cored. Though cuspy halos are found in cosmological DM-only simulations, cored halos are generally expected in theoretical models of dSph formation that account for the effect of baryons (e.g. Navarro et al. 1996; Mo & Mao 2004; Mashchenko et al. 2006; Del Popolo 2009; Di Cintio et al. 2014; Pontzen & Governato 2014; Nipoti & Binney 2015). Moreover, cored halos tend to reproduce the observations better than cuspy halos (e.g. Walker & Peñarrubia 2011; Jardel & Gebhardt 2012; Amorisco, Agnello, & Evans 2013), though this finding is still debated (see e.g. BH13). Since previous works found that the stellar component of simulated galaxies within cuspy DM halos is more resilient to tides than in cored DM halos (e.g. Peñarrubia et al. 2010), the assumption of a cored DM profile should enhance the pace at which our satellite is affected by tidal disturbances. Here we represent the initial DM halo of the dwarf with a density profile

$$\rho_{\text{DM}}(r) = \rho_{0,\text{DM}} \left(1 + \frac{r}{r_{c,\text{DM}}} \right)^{-3} e^{-\left(\frac{r}{r_{t,\text{DM}}} \right)^2}, \quad (6)$$

which can be thought of as a NFW-like profile (Navarro, Frenk, & White 1995) with scale radius $r_{c,\text{DM}}$, but with no central cusp ($d \ln \rho / d \ln r = 0$ at $r = 0$) and truncated exponentially at radii larger than $r_{t,\text{DM}}$.

In all the simulations we fixed $m = 0.71$ (the observed best-fitting Sérsic index; see Section 2), $r_{c,\text{DM}} = 3.5 \text{ kpc}^4$ and $r_{t,\text{DM}} = 6 \text{ kpc}$, while the initial stellar scale radius $r_{c,*}$,

⁴ The choice of a relatively large value of $r_{c,\text{DM}}$ is needed to reproduce the flat shape of the LOS velocity-dispersion profile observed in Fornax, under our assumption of isotropic stellar velocity distribution. A similar LOS velocity-dispersion profile can be obtained with larger values of $r_{c,\text{DM}}$, combined with higher values of DM mass, but in practice such haloes would extend far beyond the tidal limit and lose a large fraction of their particles at the beginning of the simulation. For this reason, and to limit the number of free parameters, we decided to keep the value for $r_{c,\text{DM}}$ fixed.

total stellar mass $M_* = 4\pi \int_0^\infty r^2 \rho_*(r) dr$ and total DM mass $M_{\text{DM}} = 4\pi \int_0^\infty r^2 \rho_{\text{DM}}(r) dr$ are left as free parameters.

The values of $r_{c,*}$, M_* and M_{DM} are tuned in each simulation to reproduce in the last snapshot the projected surface-density and LOS velocity-dispersion profiles of Fornax, and its observationally estimated stellar mass. For this purpose, we used the following iterative procedure.

(i) We first adopt guess values of $r_{c,*}$, M_* and M_{DM} that give good fits to the present-day projected surface-density and LOS velocity-dispersion profiles of Fornax.

(ii) When a simulation with these values of the parameters is run, its final snapshot is projected on the plane of the sky and used to measure the stellar mass within a projected radius of 1.6 kpc ($M_{*,1.6}^{\text{sim}}$), the half-light radius ($R_{\text{hl}}^{\text{sim}}$) and the LOS velocity dispersion within the half-light radius ($\sigma_{\text{LOS,hl}}^{\text{sim}}$).

(iii) New values of $r_{c,*}$, M_* and M_{DM} (here indicated with primes) are then calculated as follows:

$$\begin{aligned} r'_{c,*} &= r_{c,*} (R_{\text{hl}}^{\text{obs}}/R_{\text{hl}}^{\text{sim}})^{0.5}, \\ M'_* &= M_* (M_{*,1.6}^{\text{obs}}/M_{*,1.6}^{\text{sim}})^{0.5}, \\ M'_{\text{DM}} &= M_{\text{DM}} (\sigma_{\text{LOS,hl}}^{\text{obs}}/\sigma_{\text{LOS,hl}}^{\text{sim}}), \end{aligned}$$

where $M_{*,1.6}^{\text{obs}} = 4.3 \times 10^7 M_\odot$, $R_{\text{hl}}^{\text{obs}} = 0.6$ kpc and $\sigma_{\text{LOS,hl}}^{\text{obs}} = 12 \text{ km s}^{-1}$ are the observational estimates for Fornax (see Section 2).

Steps (ii) and (iii) are repeated until convergence (defined by the condition that the three free parameters change by less than 10%). For the simulations presented here, the above scheme converged after 2-3 iterations. It must be noted that our iterative procedure is not as robust as other more complex algorithms developed for this purpose (see e.g. Ural et al. 2015) and could potentially fail to converge if significant changes in the structure of the satellite occurred. However, given the relatively wide orbit of Fornax, in all our simulations the three parameters change by small amounts during the entire satellite evolution (see Section 4), so we believe that the simple procedure adopted here provides reliable results in the present context.

The N -body simulations have been performed with the collisionless code FVFPs (Londrillo et al. 2003; Nipoti et al. 2003), which has been specifically modified to include the fixed external potential of the MW (equations 2-4). We adopted the following values of the code parameters: minimum value of the opening parameter $\theta_{\text{min}} = 0.5$, softening parameter $\varepsilon = 10$ pc, and (constant) time-step $\Delta t = 3.2 \times 10^5$ yr. The initial equilibrium two-component satellite system is generated assuming isotropic velocity distribution: given the density distribution of each component and the corresponding total gravitational potential, the particles are assigned phase-space coordinates x , y , z , v_x , v_y , v_z (centred in the dwarf galaxy's centre of mass) using the ergodic distribution function obtained with Eddington's inversion (Binney & Tremaine 2008). The parameters of the simulations, including the number of stellar (N_*) and DM (N_{DM}) particles, are given in Table 2.

4 RESULTS

4.1 Evolution of the satellite's stellar and dark-matter components

We present here the results of three simulations (P07best, P07ecc and P07ecc_{sh}) differing in either the satellite orbit or the initial stellar and DM density distributions (see Table 2). Simulations P07best and P07ecc have the same initial DM and stellar distribution and differ only in the orbital parameters ($e = 0.13$ and $e = 0.4$, respectively). In simulation P07ecc_{sh} the satellite is placed on the more eccentric orbit (as in simulation P07ecc), but the stellar component starts with a more centrally concentrated spatial distribution than in simulation P07ecc, and a DM mass higher by a factor 1.4. In all these simulations the total stellar mass is $M_* = 5 \times 10^7 M_\odot$. The simulations are run for 12 Gyr: the final snapshot corresponds to the present day and can be compared with the observational data of Fornax.

Figures 2-4 show the spatial distribution of DM and stellar particles after 2, 7 and 12 Gyr for the simulations P07best, P07ecc and P07ecc_{sh}. In all cases the DM component develops tidal tails: the fraction of particles contained in the tidal tails is clearly higher in the simulations on the more eccentric orbit. Tidal tails are instead absent in the stellar component in all these simulations. This can be qualitatively understood considering that along the P07best orbit the minimum (pericentric) tidal radius, calculated according to the prescriptions of Allen, Moreno, & Pichardo (2006, see their appendix A) and assuming a mass for Fornax of $3 \times 10^9 M_\odot$ (see Table 2), is $r_{t,\text{min}} = 13.16$ kpc, which is large compared to the characteristic size of the stellar component of Fornax (in the initial conditions of the simulations about 99% of the stellar mass is contained within 2 kpc). The more eccentric orbit P07ecc has a minimum tidal radius $r_{t,\text{min}} = 7.36$ kpc, which is significantly smaller than that of orbit P07best, but still larger than the radius containing most of the stellar mass. So, during the satellite orbit, stars are always contained within the instantaneous tidal radius and are not expected to be significantly affected by tides. Taken at face value, the above estimates of the tidal radii are relative large also with respect to the characteristic size of the DM distribution (in the initial conditions about 90% of the DM mass is contained within $r = 7.5$ kpc), so the above simple analysis would predict moderate tidal effects also for the halo. In fact, the N -body simulations show that the DM halo develops evident tidal tails and lose a significant fraction of its mass. The stellar component is not tidally stripped, but, at least on the more eccentric orbit, its internal structure and kinematics evolve due to the variation of the gravitational potential induced by the tidal stripping of the halo.

Figures 5-7 show the intrinsic angle-averaged stellar and DM density profiles of the satellite in simulations P07best, P07ecc and P07ecc_{sh} at $t = 2, 7$ and 12 Gyr, compared to the initial ones. Figures 8-10 show, for the same simulations, the initial ($t = 0$) and final ($t = 12$ Gyr) projected number-density and LOS velocity-dispersion profiles compared to the observations. The final projected properties of the satellite are computed by assuming that the system is observed from the Sun. Given that we consider an axisymmetric MW potential, we have the freedom to fix the position of the Sun a posteriori in a circle of radius 8.5 kpc lying in the Galactic

Table 2. Initial parameters of the simulations. $r_{c,*}$: scale radius of the stellar distribution; M_* : stellar mass; M_{DM} : DM mass; M_{tot} : total mass; N_* : number of stellar particles; N_{DM} : number of DM particles; N_{tot} : total number of particles; e : orbit eccentricity. *Notes.* For simulation P07best_{flat}, in which the stellar component is initially flattened, $r_{c,*}$ refers to the spherical distribution used in the set-up of the initial conditions (see Section 4.4). In simulations P07best_{MFL} and P07ecc_{MFL} there is no distinction between stars and DM, so $r_{c,*}$ is the scale radius of the total mass distribution.

Name	$r_{c,*}$ kpc	M_* M_{\odot}	M_{DM} M_{\odot}	M_{tot} M_{\odot}	N_*	N_{DM}	N_{tot}	e
P07best	0.581	5×10^7	3×10^9	3.05×10^9	51200	1536000	1587200	0.13
P07ecc	0.581	5×10^7	3×10^9	3.05×10^9	51200	1536000	1587200	0.40
P07ecc _{sh}	0.465	5×10^7	4.2×10^9	4.25×10^9	51200	2150400	2201600	0.40
P07best _{MFL}	0.581	-	-	1.5×10^8	-	-	51200	0.13
P07ecc _{MFL}	0.581	-	-	1.5×10^8	-	-	51200	0.40
P07best _{flat}	0.581	5×10^7	2.6×10^9	2.65×10^9	51200	1331200	1382400	0.13

plane and centred in the Galactic centre. The Sun position is chosen in each simulation to obtain the best possible match with the heliocentric centre-of-mass position and systemic velocity of Fornax which are in all the simulations presented here reproduced to within 5%.

The final properties of the dwarf galaxies in the simulations are summarized in Table 3. In simulation P07best neither the DM nor the stellar distributions evolve substantially. At the end of the simulation 97.5% of the DM particles and virtually all the stellar particles are bound to the satellite. At the end of the simulation both the projected number-density and LOS velocity-dispersion profiles of the stars are very similar to the initial ones and compare well to the observations. A convenient reference radius to analyze the properties of the satellite is 1.6 kpc, which contains about 90% of the stellar mass in the initial conditions, besides corresponding approximately to the outermost point of the observed LOS velocity dispersion profile of Fornax, within which de Boer et al. (2012) estimated Fornax’s stellar mass. From the start to the end of the simulation, the DM mass within 1.6 kpc changes little, from 2.68×10^8 to $2.64 \times 10^8 M_{\odot}$. The final stellar mass within 1.6 kpc is $M_{*,1.6} \simeq 4.6 \times 10^7 M_{\odot}$, consistent within 7% with the estimate of de Boer et al. (2012).

A satellite with the same initial conditions, placed onto the more eccentric orbit (simulation P07ecc), experiences a significant evolution due to tidal forces: the surface-density profile of the stars becomes more extended and the average LOS velocity dispersion becomes lower (see Fig. 9). These changes are mainly due to the loss of mass from the DM halo, whose density profile is substantially altered over 12 Gyr of evolution (see Fig. 6). At the end of the simulation the satellite retains only 50% of the DM particles (the DM mass within 1.6 kpc is 59% of the initial value). Because of the consequent variation of the gravitational potential, the satellite reaches an equilibrium configuration characterized by a larger scale length and lower velocity dispersion (the stellar component retains 92% of its mass within 1.6 kpc). A similar behaviour was noticed in previous works studying the effects of tides on dwarf galaxies (e.g. Peñarrubia, Navarro, & McConnachie 2008). Overall, the final snapshot of simulation P07best is not a good representation of the observations: the stellar particle surface-density profile of the simulated galaxy is too extended with respect to the observed one, and the LOS velocity-dispersion profile is too low (see Fig. 9).

In order to reconcile with the observations the final properties of our simulated galaxy when placed on the more eccentric orbit, the initial conditions had to be modified, starting with a more concentrated stellar density profile and increasing the initial DM mass (model P07ecc_{sh}). As shown in Fig. 10, the final snapshot of this simulation is in good agreement with the observations. In this case, the fraction of bound DM particles at the end of the simulation is 71% (the final DM mass within 1.6 kpc is 79% of the initial value). As in simulations P07best and P07ecc, virtually all the stellar particles are bound to the object after 12 Gyr of evolution. The final stellar mass within 1.6 kpc is more than 98% of the initial value: the object expands slightly, with an associated small decrease in the central LOS velocity dispersion.

The results of simulations P07best and P07ecc_{sh} show that the present-day observed structure and kinematics of Fornax can be reproduced by a system whose stellar component varies only little during its 12 Gyr journey in the MW on observationally-motivated orbits. In particular, the simulated systems are found to be quasi-stationary in the last Gyr of evolution. This suggests that Fornax can be reasonably well modeled as an isolated system in equilibrium. The final fraction of unbound stars in the simulations is negligible, so the spectroscopic samples of Fornax stars should not be contaminated significantly by tidally stripped stars. Interestingly, baryons and DM appear to contribute similarly to the mass budget in the central regions of Fornax, suggesting that this galaxy may not be “DM dominated at all radii”, as believed to be the case for most MW dSphs.

4.2 Jeans analysis of the final snapshots

As a further test of the dynamical status of Fornax, we carried out an equilibrium mass modeling analysis of the final snapshots of simulations P07best and P07ecc_{sh}, which were shown to match well the observed properties of Fornax. Should the stellar component of the simulated systems be out of dynamical equilibrium, then we would expect to find a discrepancy between the DM mass determined from the equilibrium analysis and the “true” DM mass as measured directly from the snapshot.

The simulated stellar component is our tracer of the gravitational potential: given the LOS velocity-dispersion and surface number-density profiles measured in the final snapshots of the simulations (Figs. 8 and 10), we wish to find the total mass distribution using the spherical Jeans

equations (Binney & Mamon 1982) under the assumption that the velocity distribution of the tracers is isotropic. We model the total mass density profile as the sum of the stellar and DM density profiles. The tracers' density and mass profiles are obtained by deprojecting (assuming spherical symmetry) the Sérsic profile (equation 1) with parameters as in Table 1 and stellar mass $5 \times 10^7 M_\odot$. For the DM density profile we assume a simple model of the form

$$\rho_{\text{DM}}(r) = \rho_{0,\text{DM}} \left(1 + \frac{r}{r_{c,\text{DM}}} \right)^{-4} \quad (7)$$

(Dehnen 1993), which yields the analytic mass profile

$$M_{\text{DM}}(r) = M_{\text{DM},\infty} \left(\frac{r}{r_{c,\text{DM}} + r} \right)^3, \quad (8)$$

where $M_{\text{DM},\infty} = 4\pi\rho_{0,\text{DM}}r_{c,\text{DM}}^3/3$ is the total DM mass.

We determine the best-fitting $M_{\text{DM},\infty}$ and $r_{c,\text{DM}}$ via a χ^2 minimization. Though these two parameters are quite degenerate, we find that the DM mass enclosed within 1.6 kpc ($M_{\text{DM},1.6}$) is not significantly affected by this degeneracy ($M_{\text{DM},\infty}$ is anyway a ill-constrained quantity due to the limited spatial extent of the tracer kinematic data with respect to the extent of the DM halo). We obtain a remarkably good agreement between $M_{\text{DM},1.6}$ yielded by the equilibrium Jeans analysis and the values measured in the final snapshots of simulations P07best and P07ecc_{sh}, with a difference of at most 7%. This lends support to the fact that, at the present-day position of Fornax and along orbits compatible with literature proper motion measurements, it is reasonable to assume that tidal effects are not significant for DM determinations of this satellite galaxy within the region probed so far by the kinematic data.

4.3 Mass-follows-light models

So far we have assumed that the initial satellite's DM halo is extended. In principle, an alternative possibility is that, in the absence of an extended DM halo, tidal forces are effective in producing a flat and high LOS velocity-dispersion profile as observed (Aaronson 1983). For instance, such a model appears to provide a good match to the observed structure and kinematics of the Carina dSph (Muñoz, Majewski, & Johnston 2008). To explore this idea for the case of Fornax, we ran two additional simulations in which we make the extreme assumption that “mass follows light”. In practice, in these simulations we do not distinguish between stars and DM: the satellite is represented initially as a one-component isotropic system of total mass $M_{\text{tot}} = 1.5 \times 10^8 M_\odot$ with the same initial density profile as the stellar component of simulations P07best and P07ecc. With this choice the central LOS velocity dispersion is similar to the value measured in Fornax. However, as expected, the initial velocity-dispersion profile is much steeper than observed. We considered both the P07best orbit (simulation P07best_{MFL}) and the more eccentric orbit P07ecc (simulation P07ecc_{MFL}). The resulting spatial distribution of particles after 2, 7 and 12 Gyr are shown in Figs. 11 and 12; the corresponding intrinsic density and LOS velocity-dispersion profiles in Fig. 14.

In simulation P07best_{MFL} a small fraction ($\sim 2\%$) of the initial mass appears to be decoupled from the main body of

the galaxy, thus forming a hint of tidal tails. At the end of the evolution both the projected number-density and LOS velocity-dispersion profiles of the stars are very similar to the initial ones. Therefore, the LOS velocity dispersion profile is still significantly decreasing with radius, being just somewhat higher than the initial profile at $R > 0.6$ deg, with velocity dispersion $\approx 6 \text{ km s}^{-1}$. This is at odds with observations, in which the velocity dispersion profile is flat with values $\approx 12 \text{ km/s}$ up to $R \simeq 0.7$ deg (see Fig. 14, left-hand panels). In simulation P07ecc_{MFL} the system develops a clearer pair of tidal tails. However, also in this case the satellite loses a small fraction of the initial satellite mass budget ($\sim 3\%$), so the final density and velocity dispersion profiles are very similar to those of simulation P07best_{MFL}. High values of the final LOS velocity dispersion are found in simulation P07ecc_{MFL} only at $R > 1$ deg, far beyond the region covered by kinematic observations (see Fig. 14, right-hand panels). We note that in the orbits considered here the tidal tails developed by the satellite are never aligned along the LOS (a configuration that could enhance the LOS velocity dispersion at smaller projected radii; Klimentowski et al. 2007).

These results suggest that, even in the absence of an extended DM halo, neither the large amplitude of Fornax's velocity-dispersion profile, nor its approximately flat shape, are caused by lack of dynamical equilibrium due to tidal disturbances from the MW. In other words, Fornax's kinematic samples are not expected to be significantly contaminated by tidally stripped stars.

4.4 A flattened model

In the simulations described in the previous sections we have assumed that the satellite is initially spherical. In fact, we mentioned in Section 2 that the observed stellar component of Fornax is flattened, with observed ellipticity $\epsilon = 0.3$. The simplest interpretation of this deviation from circular symmetry is that Fornax's stellar component is intrinsically axisymmetric. Given the available observational information, the inclination of the system with respect to the LOS is unknown and it is unclear how much rotation or velocity anisotropy contribute to the observed flattening. A more realistic simulation of the evolution of Fornax in the MW should start from a non-spherically symmetric satellite and match, in the final snapshot, the observed ellipticity, together with the other observables. Clearly this is not an easy task, because intrinsic shape, inclination, rotation and anisotropy add several degrees of freedom. In the spirit of showing that the observed ellipticity can be reproduced sufficiently well with a simple model and that the results described above are not specific to spherically symmetric models, here we present, as an example, the result of an additional simulation named P07best_{flat}, which follows the orbit P07best (see Table 2).

In simulation P07best_{flat} the satellite is initially represented by an oblate (but non-rotating) stellar component and by an almost-spherical DM halo. In practice, the initial conditions are constructed as follows. We start by generating a two-component spherical, isotropic system with stellar and DM density profiles given by equations (5) and (6), respectively, with the same parameters as in simulation P07best, but $M_{\text{DM}} = 2.6 \times 10^9 M_\odot$. Each particle is characterized by

coordinates x, y, z, v_x, v_y, v_z centred in the dwarf galaxy’s centre of mass. The phase-space coordinates of the stellar⁵ particles are modified as follows: x, y, v_x and v_y are multiplied by a coefficient a , and z and v_z by a coefficient $b < a$. In practice we use $a = q^{-1/3}$ and $b = q^{2/3}$, so the final minor-to-major intrinsic axis ratio is $q = b/a$. Specifically, we adopt $q = 0.58$, so the (constant) intrinsic ellipticity is $\epsilon_i = 1 - q = 0.42$. Such a system is not in equilibrium, but we verified empirically that it is actually a quasi-equilibrium configuration. We followed the evolution of such a system in isolation with an N -body simulation, finding that an equilibrium configuration, still with ellipticity $\epsilon_i \simeq 0.41$, is reached after 1 Gyr of evolution. The DM distribution slightly adjusts itself because of the presence of the flattened stellar component, but we find that after 1 Gyr the halo is still very close to spherical symmetry. We take as initial ($t = 0$) satellite in simulation P07best_{flat} this N -body system as it is after 1 Gyr of evolution in isolation. The initial phase-space coordinates of the centre of mass of the dwarf are the same as in simulation P07best and the orientation of the system’s axes is empirically chosen so that at the end of the simulation the system is seen almost edge-on when observed from the Sun. The iterative algorithm described in Section 3 has been used to find the optimal parameters at the beginning of the simulation, including the initial intrinsic ellipticity ϵ_i , which has been updated at each iteration according to the formula

$$\epsilon'_i = \epsilon_i (\epsilon^{\text{obs}} / \epsilon^{\text{sim}})^{0.5},$$

where $\epsilon^{\text{obs}} = 0.3$ and ϵ^{sim} are the projected ellipticities calculated on observed data and in the last snapshot of the simulation (we took as initial guess $\epsilon_i = 0.3$). The initial orientation of the system is such that the equatorial plane is parallel to the LOS from the Galactic centre to the observed position of Fornax. During the simulation the vector normal to the satellite’s equatorial plane changes its direction, oscillating by several degrees, but in the last snapshot the satellite is still seen from the Sun position as approximately edge-on. The final properties of simulation P07best_{flat} are reported in Table 3.

Figure 15 shows the distribution of stellar particles in the tangent plane, centred at the coordinates of the object centre of mass, as seen from the Sun. The projected ellipticity of this simulated object is $\epsilon \simeq 0.3$, in perfect agreement with the value measured for Fornax. As it can be noted from Fig. 16 both the resulting surface number density and LOS velocity profile are also in this case in relatively good agreement with Fornax’s observed properties. The DM and stellar mass loss is similar to the P07best spherical case: less than 3% of stars and $\sim 8\%$ of DM are lost within a radius of 1.6 kpc. In Fig. 16 we also overlay the profiles of the simulated stellar component at the end of the evolution, as it would appear if seen exactly edge-on: in this case the object’s ellipticity would be $\epsilon \simeq 0.42$, but the surface-density and LOS velocity dispersion profiles would not be much different from those found projecting along the actual LOS in the simulation.

⁵ The phase-space coordinates of the DM particles are left unchanged.

Table 3. Final properties of the dwarf galaxy in the two-component simulations. $M_{*,1.6}$: stellar mass within an angle-averaged radius $r = 1.6$ kpc; $M_{\text{DM},1.6}$: DM mass within $r = 1.6$ kpc; $f_{*,1.6}$: final-to-initial stellar mass ratio within $r = 1.6$ kpc; $f_{\text{DM},1.6}$: final-to-initial DM mass ratio within $r = 1.6$ kpc.

Name	$M_{*,1.6}$ $10^7 M_\odot$	$M_{\text{DM},1.6}$ $10^8 M_\odot$	$f_{*,1.6}$	$f_{\text{DM},1.6}$
P07best	4.62	2.64	0.991	0.985
P07ecc	4.30	1.58	0.923	0.590
P07ecc _{sh}	4.70	2.95	0.975	0.787
P07best _{flat}	4.53	2.40	0.971	0.917

5 DISCUSSION AND CONCLUSIONS

In this work we simulated the dynamical evolution over a 12 Gyr orbit around the MW of a satellite, whose final structure and kinematics resemble those of the Fornax dSph. The results shown in Section 4 indicate that even assuming a relatively eccentric orbit (still within 3σ the best-fit systemic velocities estimated by P07) the effects produced by the Galactic tidal field are relatively small, and the final system is close to equilibrium in its own gravitational potential. This suggests that the assumption of dynamical equilibrium can be safely used to estimate the mass (and DM content) of Fornax and that the existing kinematic samples are not expected to be contaminated by tidally stripped stars.

Our result is robust in the sense that our models were built so to maximize the possible tidal effects, because we followed Fornax orbit for as long as 12 Gyr in a “fully grown” MW, and we considered the orbits with the smallest pericentre still consistent with direct measurements of Fornax proper motion. According to hierarchical models of galaxy formation, a system like the MW is expected to have substantially increased its DM mass over 12 Gyr and, of course, also the MW stellar components have not been in place as they are now for such a long time span. Furthermore, Fornax may have become a MW satellite more recently than 12 Gyr ago. For example, Rocha, Peter, & Bullock (2012), based on the results of the Via Lactea II simulation, propose an infall time for Fornax of 5-9 Gyr ago. Another indication that the orbital evolution of Fornax in the MW was likely shorter than 12 Gyr can be found in its very extended star formation history, with star formation having occurred until ~ 50 -100 Myr ago. It is still debated on what timescales ram-pressure stripping can remove the gaseous component of the MW dSphs progenitors; nonetheless, the observational finding that Local Group gas-rich star-forming dwarfs are mostly located beyond the estimated MW or M31 virial radius (e.g. van den Bergh 2000, Irwin et al. 2007) suggests that objects with recent star formation activity must have spent a considerable fraction of their lifetime far from the large Local Group spirals. Overall, we expect that in a more realistic set-up the effect of tides would be milder than what examined here.

As we describe the MW as a fixed gravitational potential, we neglect the effect of dynamical friction on the satellite’s orbit. As Fornax orbits in relatively low-density regions of the MW, dynamical friction is not expected to be very important. In any case, the effect of dynamical friction is to bring the satellite closer to the host’s centre: if dynamical

ical friction were accounted for, the backward in time reconstructed orbit of Fornax would be more extended than the one considered here. Also in this sense, our simulations with fixed MW potential tend to slightly overestimate the tidal effects. Moreover, a more external orbit and consequently weaker tidal effects would be obtained by assuming a less massive model for the MW, as recently suggested by Gibbons, Belokurov & Evans (2014) on the basis of the shape and extent of the Sagittarius stream.

Based on the results of the present work, we are reassured on the fact that dynamical mass estimates of Fornax derived from equilibrium dynamical models are reliable. Still, as well known, dynamical models suffer from the mass-anisotropy degeneracy, so that different combinations of DM density and stellar-anisotropy profiles can reproduce equally well the observations. Moreover, given Fornax’s observed ellipticity, additional degrees of freedom derive from the uncertainties on the intrinsic shape and rotational support of this dSph (see Hayashi & Chiba 2012 and Jardel & Gebhardt 2012, who studied axisymmetric equilibrium models of Fornax). However, while the inner DM distribution is hard to determine, the mass within 1.6 kpc (approximately the outermost point of the observed LOS velocity dispersion profile of Fornax) is believed to be more robustly constrained (BH13). Therefore, in the limits of the considered approximations (initial spherical symmetry and isotropic velocity distribution, with the exception of simulation P07best_{flat}), our simulations can be also used to estimate Fornax’s DM mass over the scales probed by the existing kinematic datasets. The simulations that successfully reproduce Fornax’s observables have a dark-to-luminous mass ratio within 1.6 kpc in the range 5 – 6 (see Table 3). Measuring the same ratio within 3 kpc yields values in the range 16 – 18. We confirm that Fornax is amongst the least DM dominated dSphs, and we suggest that baryons and DM may contribute similarly to the mass budget in Fornax’s central regions. In the near future we plan to extend the present analysis to other dSphs for which the orbital parameters are sufficiently well constrained.

ACKNOWLEDGMENTS

The authors thank M. Breddels for providing Fornax’s LOS velocity dispersion profile measured in elliptical annuli and the referee, M. Wilkinson, for useful comments. GB thanks the INAF - Bologna for the hospitality during part of this work and gratefully acknowledges support through a Marie-Curie action Intra European Fellowship, funded by the European Union Seventh Framework Program (FP7/2007-2013) under Grant agreement number PIEF-GA-2010-274151, as well as the financial support by the Spanish Ministry of Economy and Competitiveness (MINECO) under the Ramon y Cajal Programme (RYC-2012-11537). AS acknowledges financial support from PRIN INAF 2011 “Multiple populations in globular clusters: their role in the Galaxy assembly” (PI E. Carretta). CN thanks the Instituto de Astrofísica de Canarias for the hospitality and acknowledges financial support from PRIN MIUR 2010-2011, project “The Chemical and Dynamical Evolution of the Milky Way and Local Group Galaxies”, prot. 2010LY5N2T.

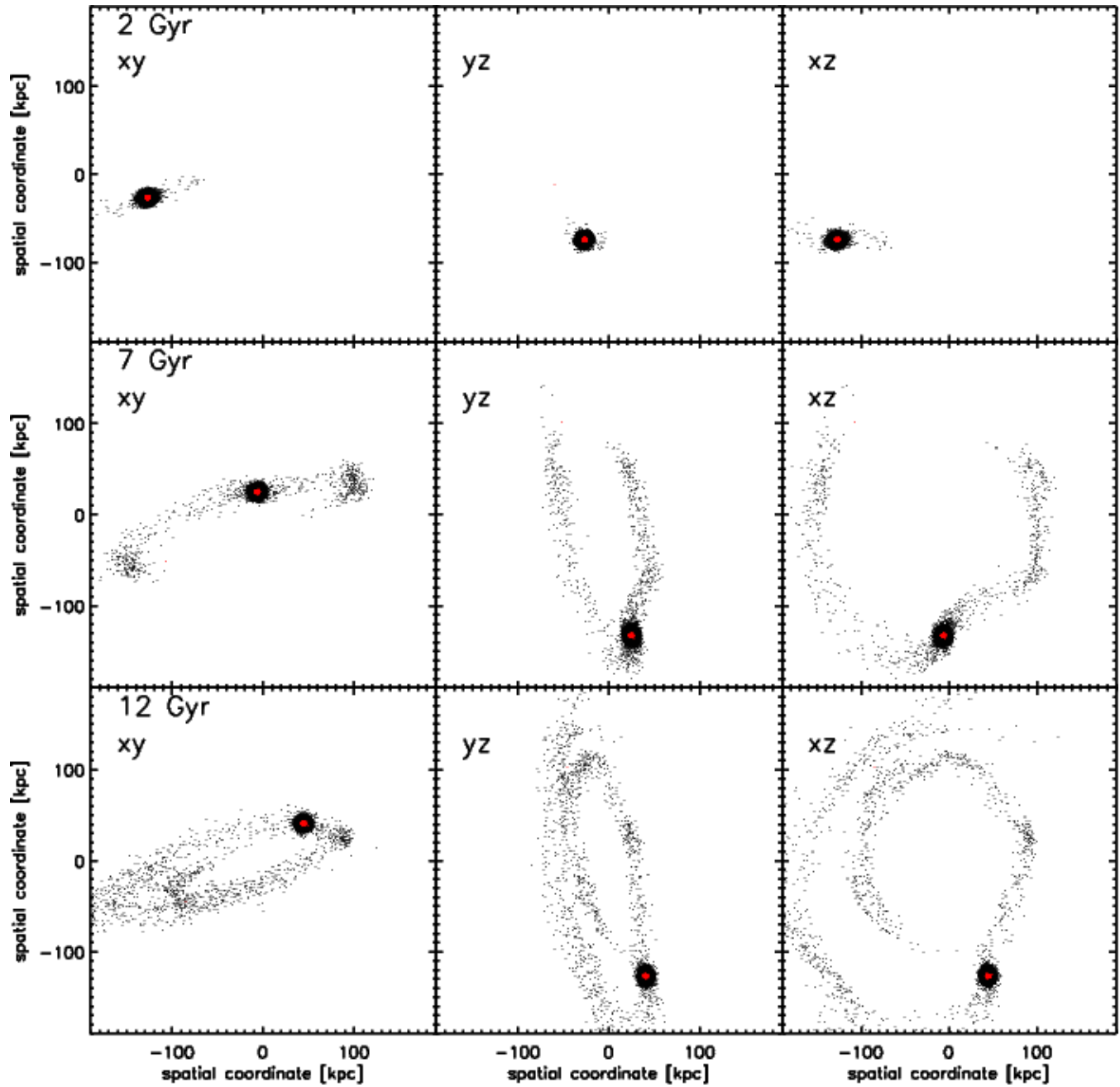


Figure 2. Distribution of DM (black) and stellar (red) particles of the satellite galaxy as seen in the x - y , y - z , and x - z planes (from left to right) for simulation P07best, after 2, 7 and 12 Gyr of evolution (from top to bottom). Here x , y and z are Cartesian Galactocentric coordinates in units of kpc (z is orthogonal to the Galactic plane). For convenience we plot one every thirty DM particles.

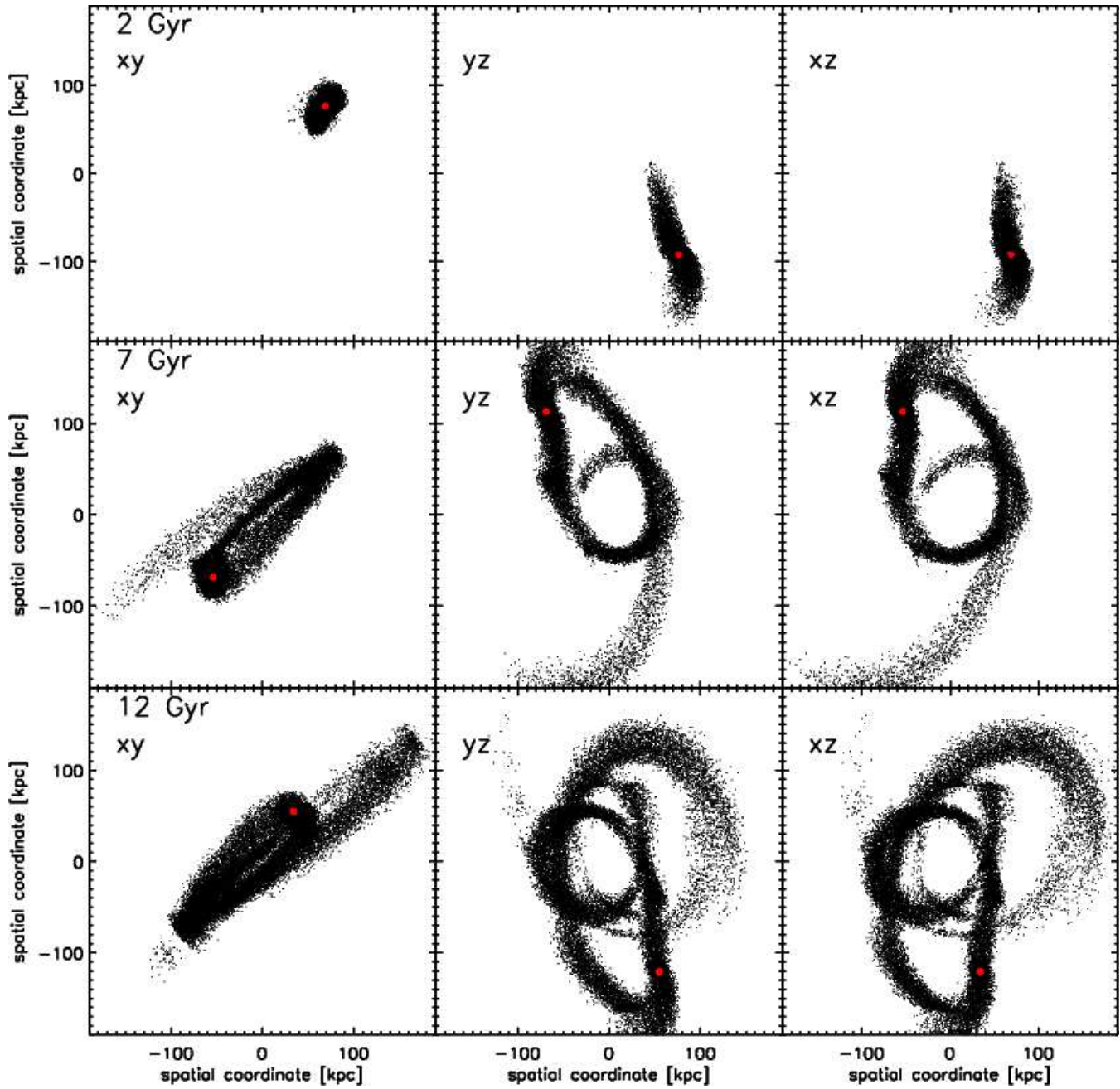


Figure 3. Same as Fig. 2, but for simulation P07ecc.

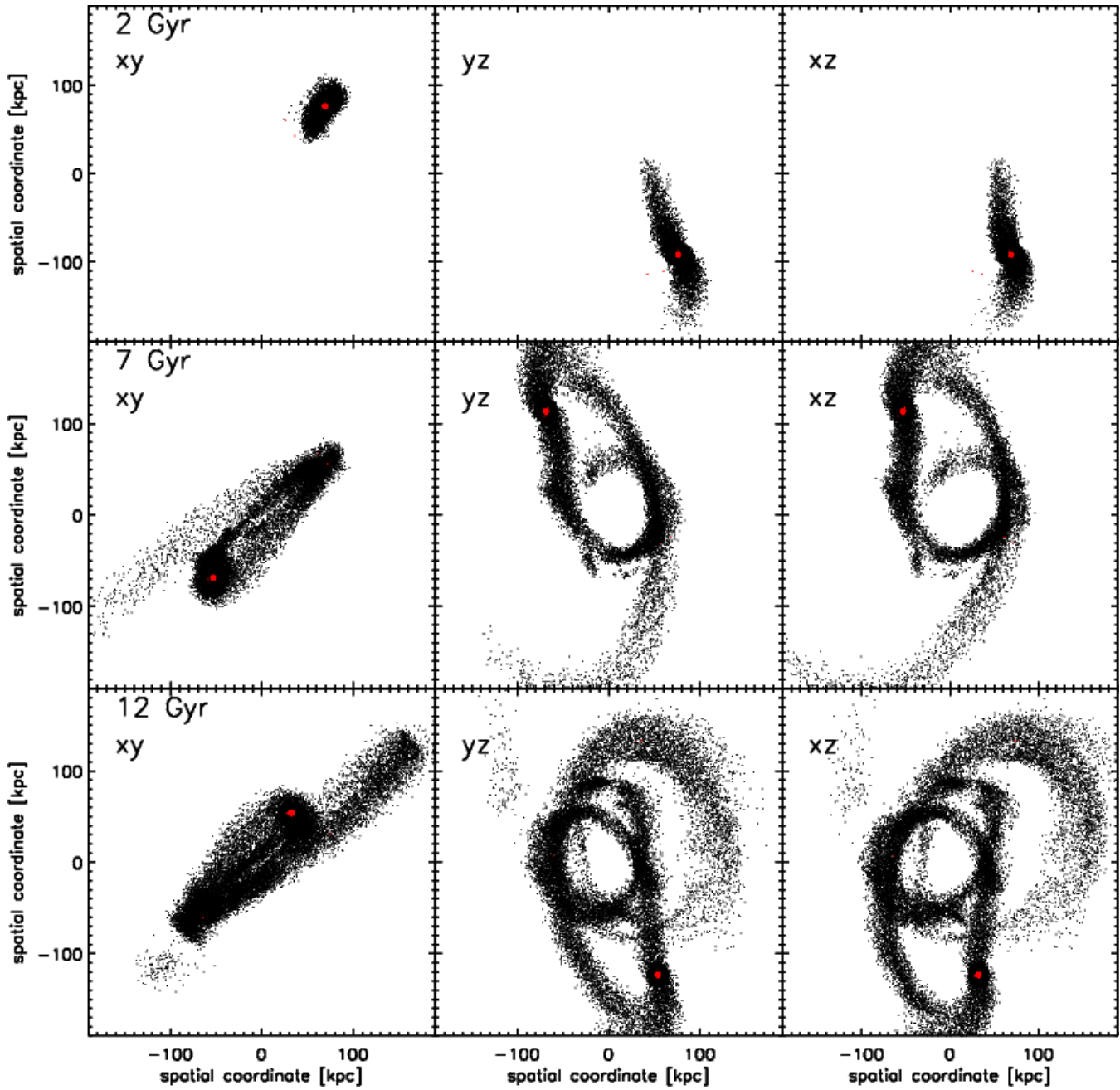


Figure 4. Same as Fig. 2, but for simulation P07ecc_{sh}

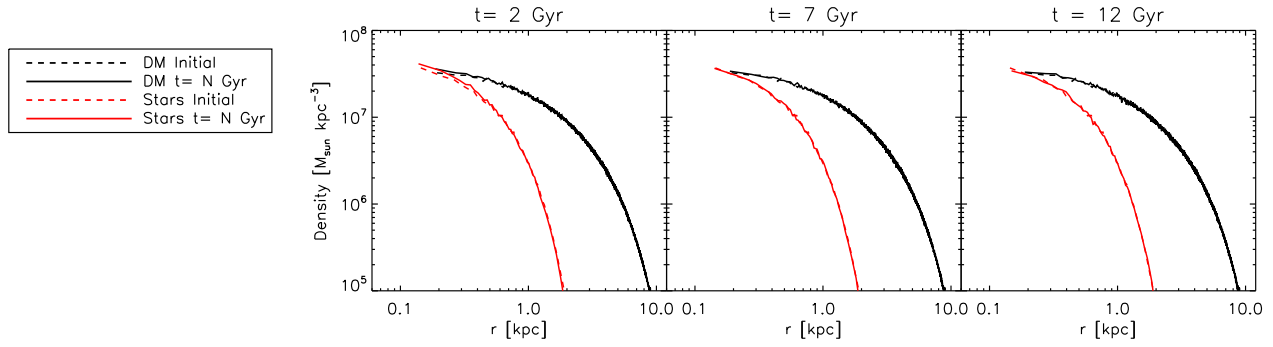


Figure 5. Angle-averaged density profiles of DM (black) and stellar (red) particles for three snapshots, at 2, 7 and 12 Gyr, for the simulation P07best (solid lines) as compared to the initial conditions (dashed lines).

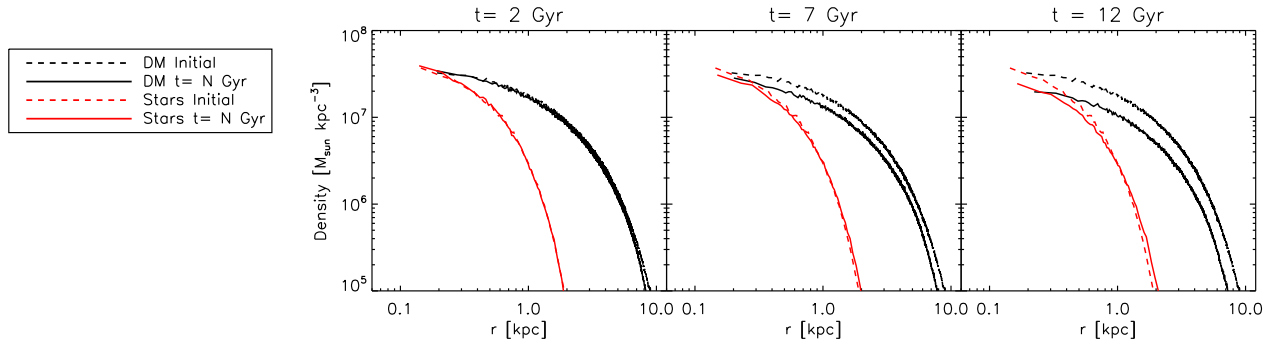


Figure 6. Same as Fig. 5, but for simulation P07ecc.

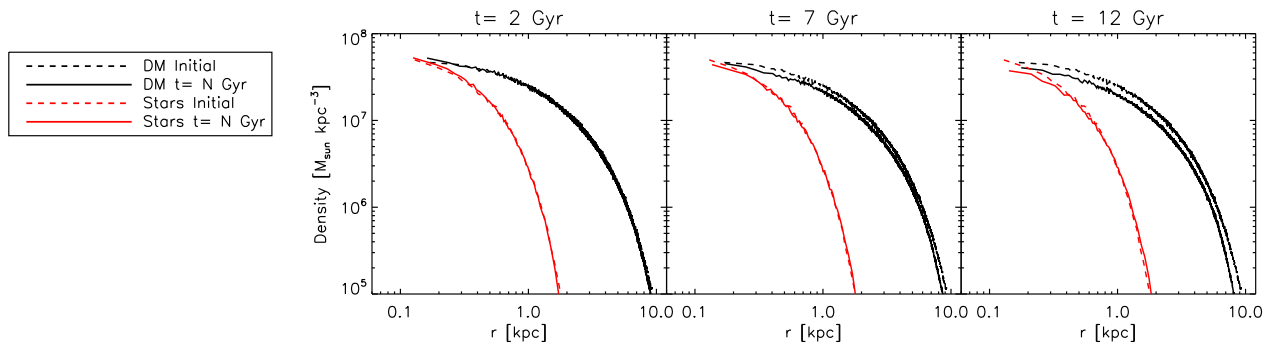


Figure 7. Same as Fig. 5, but for simulation P07eccsh.

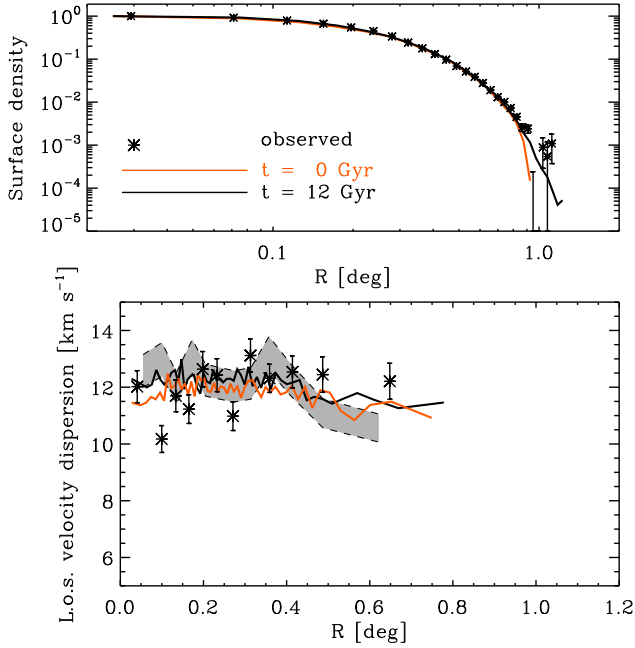


Figure 8. Surface number-density (normalized to the central value; top panel) and LOS velocity-dispersion (bottom panel) profiles of the stellar component of the P07best model. The orange and black lines indicate the initial conditions ($t=0$) and the final properties ($t = 12$ Gyr), respectively. The observed surface number-density profile from Battaglia et al. (2006) and LOS velocity-dispersion profile from BH13 are shown as black asterisks with error bars. The grey band in the bottom panel refers to the LOS velocity-dispersion profile from the 12 Gyr snapshot when using a similar number of stellar particles and binning as done by BH13 for the observations (3000 particles, 250 per bin).

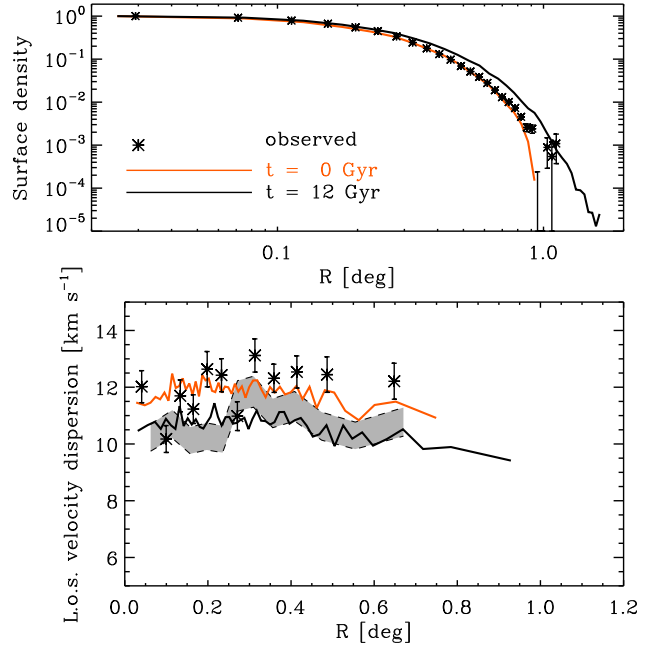


Figure 9. Same as Fig. 8, but for the P07ecc model.

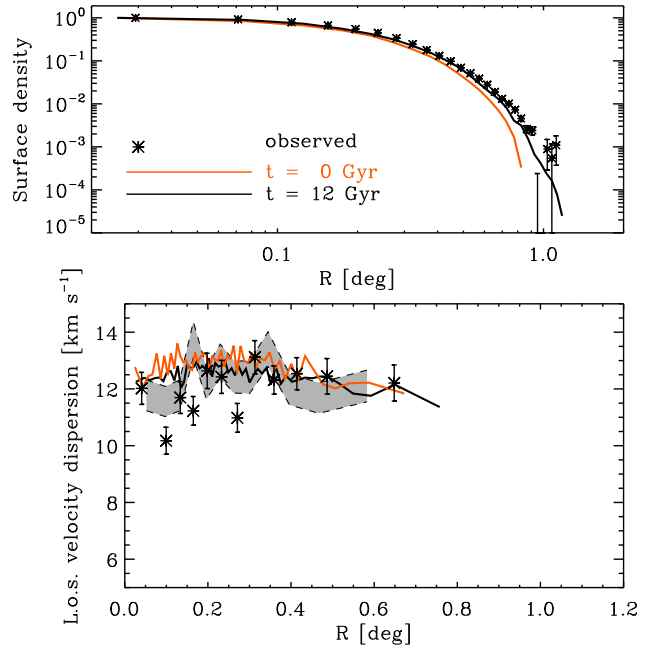


Figure 10. Same as Fig. 8, but for the P07ecc_{sh} model.

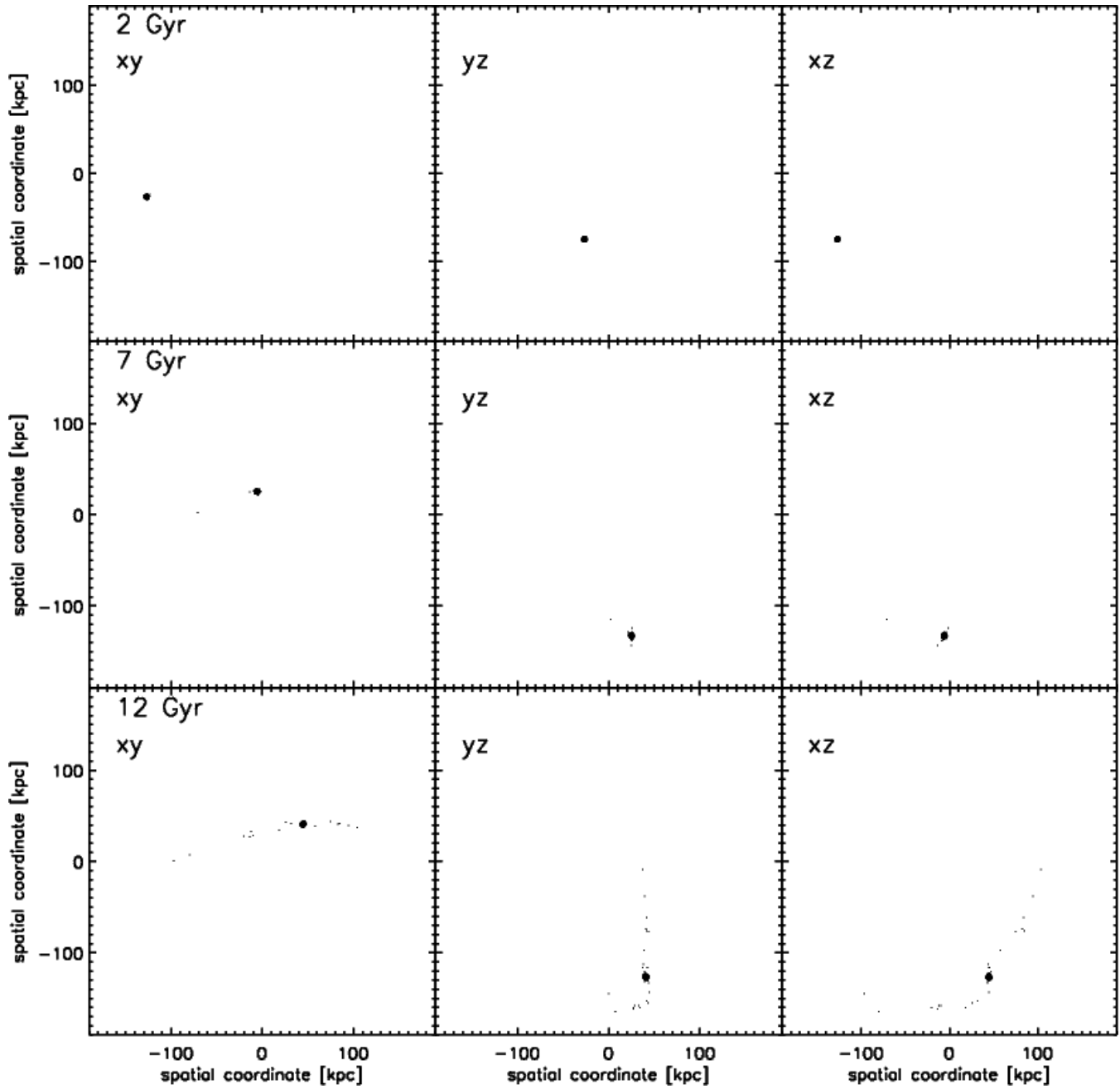


Figure 11. Same as Fig. 2, but for simulation P07best_{MFL}. Here mass follows light, so we do not distinguish between stellar and DM particles.

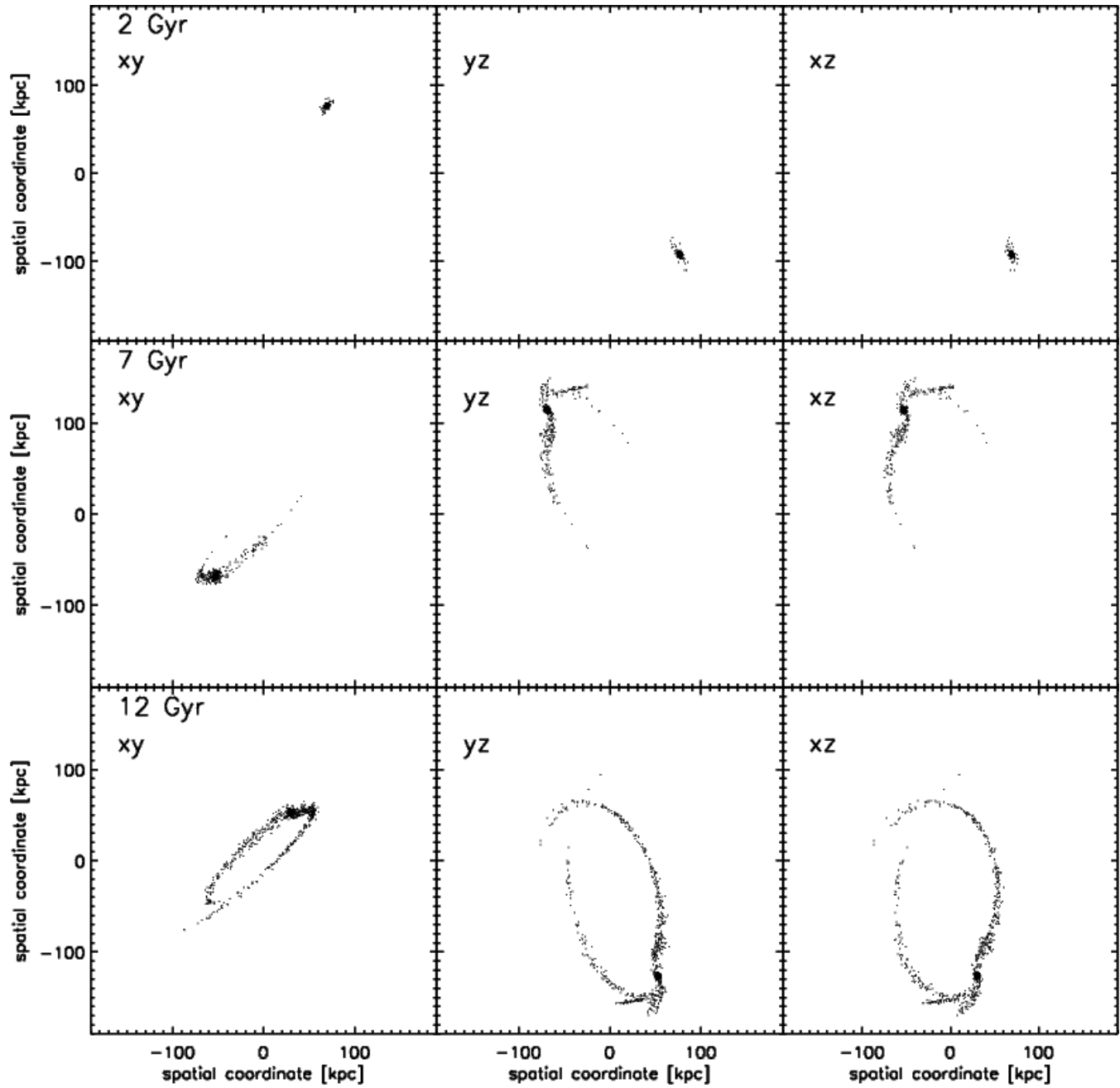


Figure 12. Same as Fig. 11, but for simulation P07ecc_{MFL}.

This paper has been typeset from a \LaTeX file prepared by the author.

REFERENCES

- Aaronson M., 1983, *ApJ*, 266, L11
- Ackermann M., et al., 2014, *PhRvD*, 89, 042001
- Allen C., Moreno E., Pichardo B., 2006, *ApJ*, 652, 1150
- Allen C., Moreno E., Pichardo B., 2008, *ApJ*, 674, 237
- Amorisco N. C., Agnello A., Evans N. W., 2013, *MNRAS*, 429, L89
- Barber C., Starkenburg E., Navarro J. F., McConnachie A. W., 2015, *MNRAS*, 447, 1112
- Bate N. F., McMonigal B., Lewis G. F., Irwin M. J., Gonzalez-Solares E., Shanks T., Metcalfe N., 2015, *MNRAS*, in press (arXiv:1507.06654)
- Battaglia G., et al., 2006, *A&A*, 459, 423
- Battaglia G., Helmi A., Tolstoy E., Irwin M., Hill V., Jablonka P., 2008, *ApJ*, 681, L13
- Battaglia G., Tolstoy E., Helmi A., Irwin M., Parisi P., Hill V., Jablonka P., 2011, *MNRAS*, 411, 1013
- Battaglia G., Irwin M., Tolstoy E., de Boer T., Mateo M., 2012, *ApJ*, 761, L31
- Battaglia G., Helmi A., Breddels M., 2013, *NewAR*, 57, 52
- Binney J., Mamon G. A., 1982, *MNRAS*, 200, 361
- Binney J., Tremaine S., 2008, *Galactic Dynamics 2nd Ed.*, Princeton University Press, Princeton
- Breddels M. A., Helmi A., 2013, *A&A*, 558, A35 (BH13)
- Breddels M. A., Helmi A., van den Bosch R. C. E., van de Ven G., Battaglia G., 2013, *MNRAS*, 433, 3173
- Choi P. I., Guhathakurta P., Johnston K. V., 2002, *AJ*, 124, 310
- Coleman M., Da Costa G. S., Bland-Hawthorn J., Martínez-Delgado D., Freeman K. C., Malin D., 2004, *AJ*, 127, 832
- Coleman M. G., Da Costa G. S., Bland-Hawthorn J., Freeman K. C., 2005, *AJ*, 129, 1443
- Crnojević D., et al., 2014, *MNRAS*, 445, 3862
- de Boer T. J. L., et al., 2012, *A&A*, 544, A73
- de Boer T. J. L., Tolstoy E., Saha A., Olszewski E. W., 2013, *A&A*, 551, A103
- Dehnen W., 1993, *MNRAS*, 265, 250
- Del Popolo A., 2009, *ApJ*, 698, 2093
- Di Cintio A., Brook C. B., Macciò A. V., Stinson G. S., Knebe A., Dutton A. A., Wadsley J., 2014, *MNRAS*, 437, 415
- Dinescu D. I., Majewski S. R., Girard T. M., Cudworth K. M., 2000, *AJ*, 120, 1892
- Dinescu D. I., Keeney B. A., Majewski S. R., Girard T. M., 2004, *AJ*, 128, 687
- Gibbons S. L. J., Belokurov V., Evans N. W., 2014, *MNRAS*, 445, 3788
- Hayashi K., Chiba M., 2012, *ApJ*, 755, 145
- Hernquist L., 1990, *ApJ*, 356, 359
- Ibata R. A., Gilmore G., Irwin M. J., 1994, *Natur*, 370, 194
- Irwin M., Hatzidimitriou D., 1995, *MNRAS*, 277, 1354
- Irwin M. J., et al., 2007, *ApJ*, 656, L13
- Jardel J. R., Gebhardt K., 2012, *ApJ*, 746, 89
- Johnston K. V., Spergel D. N., Hernquist L., 1995, *ApJ*, 451, 598
- Kazantzidis S., Lokas E. L., Callegari S., Mayer L., Moustakas L. A., 2011, *ApJ*, 726, 98
- Kleyna J. T., Wilkinson M. I., Evans N. W., Gilmore G., 2001, *ApJ*, 563, L115
- Klimentowski J., Lokas E. L., Kazantzidis S., Prada F., Mayer L., Mamon G. A., 2007, *MNRAS*, 378, 353
- Klimentowski J., Lokas E. L., Kazantzidis S., Mayer L., Mamon G. A., Prada F., 2009, *MNRAS*, 400, 2162
- Klypin A., Kravtsov A. V., Valenzuela O., Prada F., 1999, *ApJ*, 522, 82
- Koch A., Kleyna J. T., Wilkinson M. I., Grebel E. K., Gilmore G. F., Evans N. W., Wyse R. F. G., Harbeck D. R., 2007, *AJ*, 134, 566
- Lima Neto G. B., Gerbal D., Márquez I., 1999, *MNRAS*, 309, 481
- Lokas E. L., 2009, *MNRAS*, 394, L102
- Londrillo P., Nipoti C., Ciotti L., 2003, *Memorie della Società Astronomica Italiana Supplementi*, 1, 18
- Mashchenko S., Couchman H. M. P., Wadsley J., 2006, *Natur*, 442, 539
- Mateo M. L., 1998, *ARA&A*, 36, 435
- Mateo M., Olszewski E., Welch D. L., Fischer P., Kunkel W., 1991, *AJ*, 102, 914
- Mateo M., Olszewski E. W., Walker M. G., 2008, *ApJ*, 675, 201
- Mayer L., Governato F., Colpi M., Moore B., Quinn T., Wadsley J., Stadel J., Lake G., 2001, *ApJ*, 559, 754
- McConnachie A. W., Ferguson A. M. N., Irwin M. J., Dubinski J., Widrow L. M., Dotter A., Ibata R., Lewis G. F., 2010, *ApJ*, 723, 1038
- McMonigal B., et al., 2014, *MNRAS*, 444, 3139
- Méndez R. A., Costa E., Gallart C., Pedreros M. H., Moyano M., Altmann M., 2011, *AJ*, 142, 93
- Miyamoto M., Nagai R., 1975, *PASJ*, 27, 533
- Mo H. J., Mao S., 2004, *MNRAS*, 353, 829
- Moore B., Ghigna S., Governato F., Lake G., Quinn T., Stadel J., Tozzi P., 1999, *ApJ*, 524, L19
- Muñoz R. R., et al., 2006, *ApJ*, 649, 201
- Muñoz R. R., Majewski S. R., Johnston K. V., 2008, *ApJ*, 679, 346
- Navarro J. F., Frenk C. S., White S. D. M., 1995, *MNRAS*, 275, 720 (NFW)
- Navarro J. F., Eke V. R., Frenk C. S., 1996, *MNRAS*, 283, L72
- Nipoti C., Londrillo P., Ciotti L., 2003, *MNRAS*, 342, 501
- Nipoti C., Binney J., 2015, *MNRAS*, 446, 1820
- Olszewski E. W., Mateo M., Harris J., Walker M. G., Coleman M. G., Da Costa G. S., 2006, *AJ*, 131, 912
- Peñarrubia J., Navarro J. F., McConnachie A. W., 2008, *ApJ*, 673, 226
- Peñarrubia J., Navarro J. F., McConnachie A. W., Martin N. F., 2009, *ApJ*, 698, 222
- Peñarrubia J., Benson A. J., Walker M. G., Gilmore G., McConnachie A. W., Mayer L., 2010, *MNRAS*, 406, 1290
- Piatek S., Pryor C., Olszewski E. W., Harris H. C., Mateo M., Minniti D., Tinney C. G., 2003, *AJ*, 126, 2346
- Piatek S., Pryor C., Bristow P., Olszewski E. W., Harris H. C., Mateo M., Minniti D., Tinney C. G., 2007, *AJ*, 133, 818
- Pietrzyński G., Górski M., Gieren W., Ivanov V. D., Bresolin F., Kudritzki R.-P., 2009, *AJ*, 138, 459
- Pontzen A., Governato F., 2014, *Natur*, 506, 171

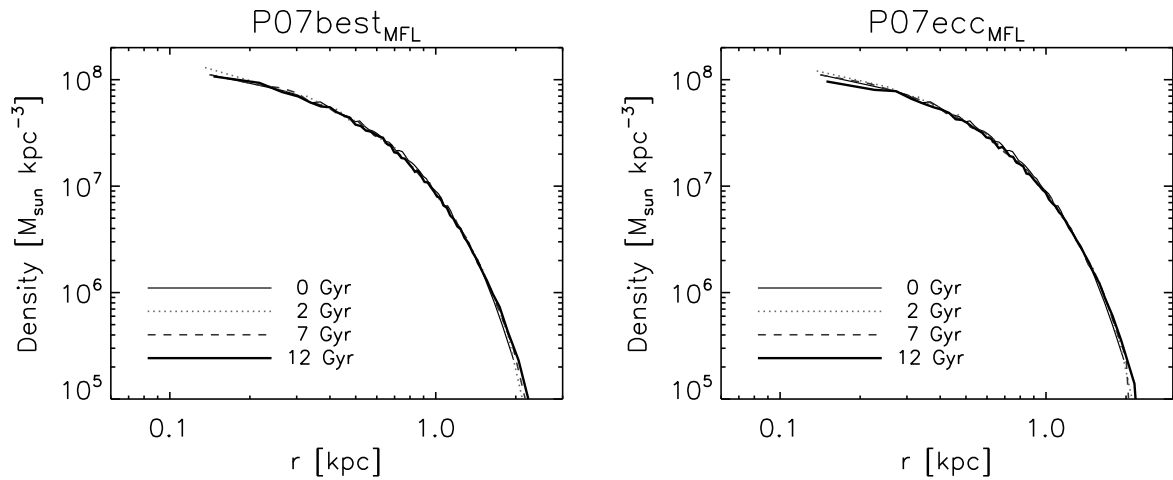


Figure 13. Angle-averaged density profiles for four snapshots, at 0, 2, 7 and 12 Gyr, for the P07best_{MFL} (left) and P07ecc_{MFL} (right) models. Here mass follows light, so we do not distinguish between stars and DM.

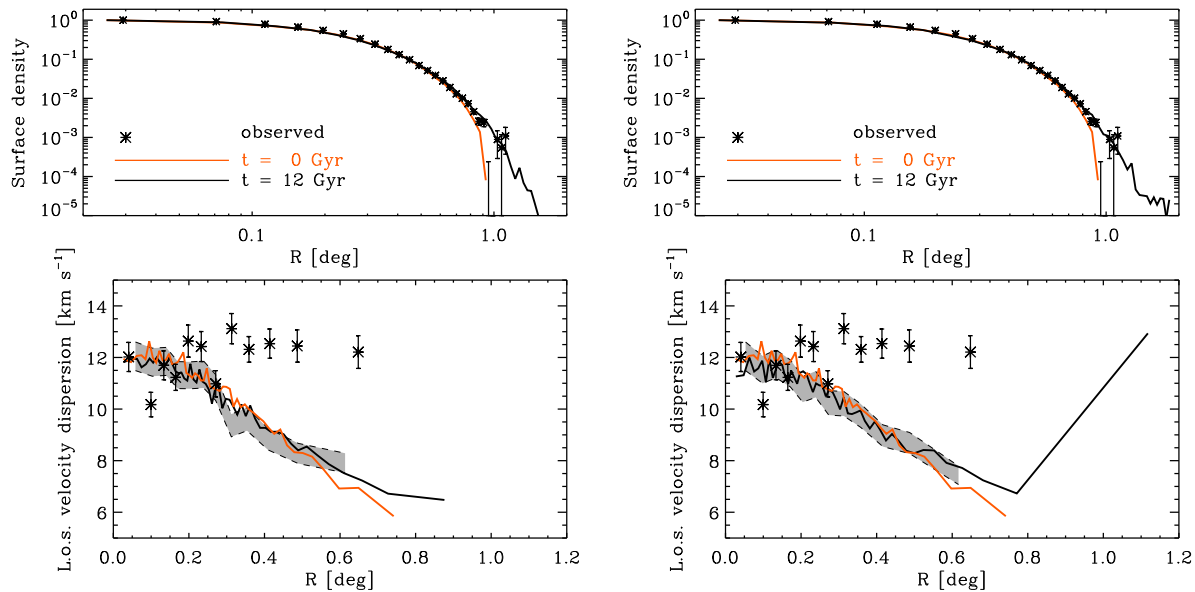


Figure 14. As in Fig. 8, but for the P07best_{MFL} (left) and P07ecc_{MFL} (right) model.

Read J. I., Wilkinson M. I., Evans N. W., Gilmore G., Kleyna J. T., 2006, *MNRAS*, 367, 387
 Richardson T., Fairbairn M., 2014, *MNRAS*, 441, 1584
 Rocha M., Peter A. H. G., Bullock J., 2012, *MNRAS*, 425, 231
 Roderick T. A., Jerjen H., Mackey A. D., Da Costa G. S., 2015, *ApJ*, 804, 134
 Saviane I., Held E. V., Bertelli G., 2000, *A&A*, 355, 56
 Sawala T., et al., 2014, preprint (arXiv:1406.6362)
 Sérsic J. L., 1968, *Atlas de galaxias australes*. Observatorio Astronomico, Cordoba (Argentina)
 Sohn S. T., et al., 2007, *ApJ*, 663, 960
 Sohn S. T., Besla G., van der Marel R. P., Boylan-Kolchin M., Majewski S. R., Bullock J. S., 2013, *ApJ*, 768, 139
 Stetson P. B., Hesser J. E., Smecker-Hane T. A., 1998,

PASP, 110, 533
 Strigari L. E., 2013, *PhR*, 531, 1
 Tomozeiu M., Mayer L., Quinn T., 2015, preprint (arXiv:1506.02140)
 Ural U., Wilkinson M. I., Read J. I., Walker M. G., 2015, *NatCo*, 6, 7599
 van den Bergh S., 2000, *CAS*, 35,
 Walker M., 2013, in *Planets Stars, and Stellar Systems*, Vol. 5, ed. T. Oswalt, & G. Gilmore, Springer, Berlin, 1039
 Walker M. G., Peñarrubia J., 2011, *ApJ*, 742, 20
 Walker M. G., Mateo M., Olszewski E. W., Bernstein R., Wang X., Woodroffe M., 2006, *AJ*, 131, 2114
 Walker M. G., Mateo M., Olszewski E. W., Gnedin O. Y., Wang X., Sen B., Woodroffe M., 2007, *ApJ*, 667, L53
 Walker, M. G., Mateo, M., & Olszewski, E. W. 2008, *ApJL*

, 688, L75
 Walker M. G., Mateo M., Olszewski E. W., 2009, AJ, 137,
 3100
 Zolotov A., et al., 2012, ApJ, 761, 71

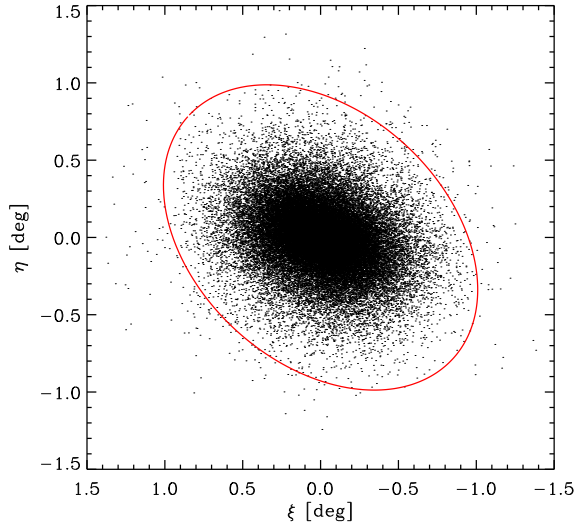


Figure 15. Spatial distribution of stellar particles in simulation P07best_{flat} projected in the tangent plane as seen from the Sun. The ellipse has the ellipticity, position angle and nominal King tidal radius as in measured by B06 (see Table 1).

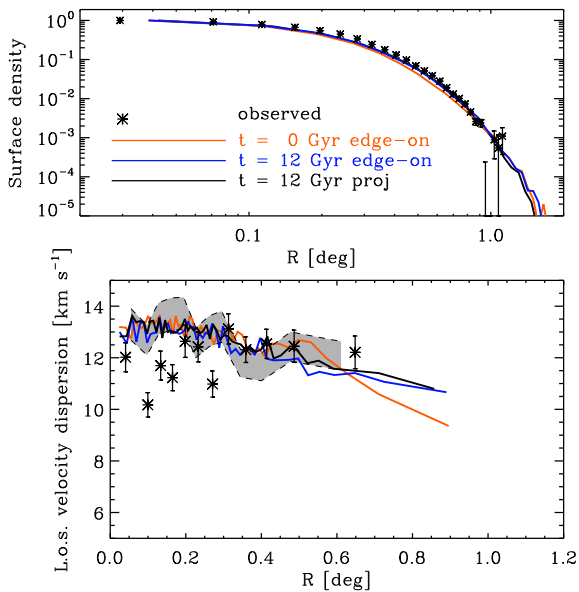


Figure 16. As in Fig. 8, but for the P07best_{flat} model. The black curves show the profiles as seen from the Sun. The orange and blue lines show the profiles of the initial and final snapshots, as seen edge-on.